

Article

Behavior Prediction and Inverse Design for Self-Rotating Skipping Ropes Based on Random Forest and Neural Network

Yunlong Qiu, Haiyang Wu, Yuntong Dai  and Kai Li * 

School of Civil Engineering, Anhui Jianzhu University, Hefei 230601, China; ylqiu@stu.ahjzu.edu.cn (Y.Q.); hywu@stu.ahjzu.edu.cn (H.W.); daiytmechanics@ahjzu.edu.cn (Y.D.)

* Correspondence: kli@ahjzu.edu.cn

Abstract: Self-oscillatory systems have great utility in energy harvesting, engines, and actuators due to their ability to convert ambient energy directly into mechanical work. This characteristic makes their design and implementation highly valuable. Due to the complexity of the motion process and the simultaneous influence of multiple parameters, computing self-oscillatory systems proves to be challenging, especially when conducting inverse parameter design. To simplify the computational process, a combined approach of Random Forest (RF) and Backpropagation Neural Network (BPNN) algorithms is employed. The example used is a self-rotating skipping rope made of liquid crystal elastomer (LCE) fiber and a mass block under illumination. Numerically solving the governing equations yields precise solutions for the rotation frequency of the LCE skipping rope under various system parameters. A database containing 138,240 sets of parameter conditions and their corresponding rotation frequencies is constructed to train the RF and BPNN models. The training outcomes indicate that RF and BPNN can accurately predict the self-rotating skipping rope frequency under various parameters, demonstrating high stability and computational efficiency. This approach allows us to discover the influences of distinct parameters on the rotation frequency as well. Moreover, it is capable of inverse design, meaning it can derive the corresponding desired parameter combination from a given rotation frequency. Through this study, a deeper understanding of the dynamic behavior of self-oscillatory systems is achieved, offering a new approach and theoretical foundation for their implementation and construction.



Citation: Qiu, Y.; Wu, H.; Dai, Y.; Li, K. Behavior Prediction and Inverse Design for Self-Rotating Skipping Ropes Based on Random Forest and Neural Network. *Mathematics* **2024**, *12*, 1019. <https://doi.org/10.3390/math12071019>

Keywords: self-rotation; liquid crystal elastomer; light powered; Random Forest; Backpropagation Neural Network

MSC: 34; 65; 74

Academic Editors: Róbert Szabolcsi and Péter Gáspár

Received: 2 March 2024

Revised: 24 March 2024

Accepted: 27 March 2024

Published: 28 March 2024



Copyright: © 2024 by the authors. Licensee MDPI, Basel, Switzerland. This article is an open access article distributed under the terms and conditions of the Creative Commons Attribution (CC BY) license (<https://creativecommons.org/licenses/by/4.0/>).

1. Introduction

Self-excited motion plays a pivotal role in applications by allowing systems to offset damping losses by drawing energy from the ambient energy [1–3], negating the requirement for intricate control mechanisms or external power supplies [4–9]. This motion's stability is notable, as its frequency and amplitude are determined by the system's intrinsic properties rather than state parameters [10]. This unique aspect opens up possibilities in engineering across diverse domains such as soft robotics [11], actuators [12], dampers [13], biomimetic devices [14], energy harvesting [15], nanotechnology [16], and mechanized logistics [17].

Recently, there has been an increase in the development of self-oscillating systems crafted from materials that react to stimuli, including but not limited to hydrogels [14,18,19], ionic gels [20], dielectric elastomers [21], and liquid crystal elastomers (LCEs) [22–27]. By using these materials, a variety of self-excited motion patterns have been demonstrated, including rolling [28–31], bending [32–35], vibration [36,37], telescoping [38,39], torsion [40,41], self-floating [42], swinging [43], swimming [44], buckling [45–47], jumping [48–50], rotation [51–53], chaos [54], and reverse [55,56]. Even several coupled self-

excited oscillators that can move synchronously are proposed [57]. Typically, the nonlinear feedback mechanisms are responsible for these self-excited motion patterns. For instance, self-masking [58], coupling of large deformation to chemical reactions [59–61], and photothermal surface tension gradients [62,63] are included. Among stimuli-responsive materials, optically responsive materials have garnered significant attention due to their exceptional properties such as environmental friendliness, remote control capabilities, and immediacy [20,27,64,65]. LCE stands out as one of the leading examples in this category.

The reality is that the analysis and design of self-oscillatory systems come with certain difficulties and complexities. Conventional analytical methods typically involve constructing a nonlinear dynamic model and deriving the governing equations through numerical computations. Nevertheless, the nonlinear, chaotic, and unstable dynamic behaviors of self-oscillatory systems make rapid behavior prediction unfeasible. Determining the appropriate parameter values is also challenging because self-oscillatory systems are difficult to understand based on the desired system behavior. When looking for the appropriate parameter values, it is essential to consider the dynamic characteristics of the system and the application requirements. Self-oscillatory systems are complex, making it challenging to assess the significance of the internal parameters. Finding a simple and quick approach to handle the analysis and design of self-oscillatory systems is crucial.

Taking the LCE self-rotating skipping rope as an example, this paper utilizes Random Forest (RF) and Backpropagation Neural Network (BPNN) algorithms for behavior prediction and inverse design. Machine learning techniques such as RF and BPNN are effective in forecasting outcomes for regression [66,67] and classification [68,69] tasks. RF and BPNN can capture complex nonlinear relationships [70] between input features and target variables. This is accompanied by merits such as interpretability, the ability to handle high-dimensional data and feature interactions, and resistance to overfitting. The traditional numerical solution method allows for obtaining the exact solution for the nonlinear dynamics model of the system, and provides the dataset necessary for training and testing the algorithm. Combining the advantages of the RF algorithm for processing classification issues and the BPNN algorithm for regression prediction, after hyperparameter training and tuning, we can predict the rotation frequency of the LCE skipping rope [71] and reverse engineer its parameter combinations based on known conditions. The outcomes of behavior prediction and inverse design validate the accuracy of this approach. In summary, several factors need to be taken into account when analyzing and designing self-oscillatory systems, including the dynamic characteristics of the system, parameter estimation, and control strategies. Different methods and techniques may be required to solve problems based on varying application requirements. The behavior prediction and inverse design based on RF and BPNN algorithms proposed in this paper provide a simple and effective approach for the analysis and design of self-oscillatory systems.

This document is organized as follows. Section 2 introduces the derivation of governing equations from the nonlinear dynamics model of the LCE skipping rope under steady illumination [71]. Section 3 presents the training results of RF and BPNN algorithms along with the discussion on their generalization capabilities. Section 4 utilizes predicted results to elucidate how the systematic parameters affect the rotation frequency of the self-rotating skipping rope. The effectiveness of inverse design is further confirmed in Section 5. Section 6 provides the conclusions in the end.

2. Model and Theoretical Framework

Firstly, we provide the theoretical framework for a skipping rope exposed to constant illumination. Secondly, we utilize the moment of momentum theorem to formulate the equations governing its motion. The evolution of the *cis-isomer* ratio in the LCE fiber, dimensionless treatment, and the traditional numerical solution for differential governing equation with variable coefficients are among them.

2.1. Rotational Dynamics of a Self-Rotating Skipping Rope

The optically activated self-rotating LCE fiber system [71], which is depicted in Figure 1, operates exposed to constant light. The ends of the LCE fiber are fixed, and a mass block with mass m is adhered to its middle portion. The distance between the two hinges is represented by $2D$. In the reference state shown in Figure 1a, the original length of the LCE fiber is $2L_0$. To simplify the analysis, we only consider the damping experienced by the block. In this analysis, the LCE fiber's mass is considered to be negligible. The LCE fiber's photosensitive azobenzene liquid crystal molecules align parallel to the fiber's longitudinal direction. It is widely recognized that under illumination, these molecules transit from a linear *trans* state to a bent *cis* state, as illustrated in Figure 1b. This molecular reconfiguration results in the contraction of the LCE fiber [72]. The yellow-colored areas in the initial state (Figure 1b) and current state (Figure 1c) stand for the illumination zone, and β is utilized to signify the illumination range. Constant parallel light is projected along the x -axis direction. Because of light absorption, the light intensity in the LCE fiber varies along its thickness. The relationship between the *cis*-to-*trans* and *trans*-to-*cis* absorption coefficients determines the depth of light penetration, typically around 100 microns [73]. To simplify, the LCE fiber with a radius much smaller than the depth of light penetration is selected, and any light attenuation in both air and the LCE fiber is ignored. Based on this, light is instantly and uniformly distributed throughout the fiber. Figure 1d is a simple diagram of machine learning.

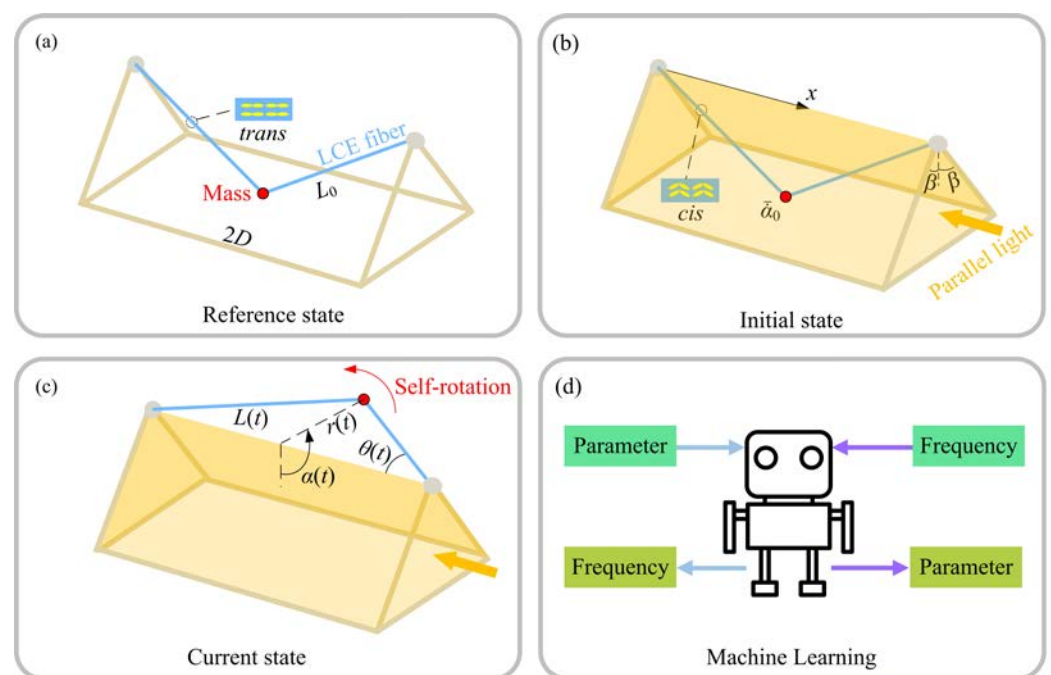


Figure 1. Schematic diagram of an LCE self-rotating skipping rope system consisting of an optically-responsive LCE fiber, a mass block, and a rod with two hinges: (a) Reference state, (b) Initial state, (c) Current state, (d) Machine learning.

The mass block is initially positioned at an angle α_0 . Subsequently, the block starts to descend from static due to the gravitational force. During the rotation, the position of the block is denoted by $\alpha(t)$, the length of the LCE fiber is indicated by $2L(t)$, and the position of the fiber is denoted by $\theta(t)$. The length between the block and the x -axis is labeled $r(t)$. When the LCE fiber is exposed to light, the contraction of the LCE fiber occurs due to the *trans*-to-*cis* transition of azobenzene liquid crystal molecules. Conversely, when the LCE fiber is in the dark, the contraction recovers due to the *cis*-to-*trans* transition of the azobenzene liquid crystal molecules. The variation of length results in shifting of the

block’s gravitational energy, and the light energy is harvested to counteract energy losses and maintain the rotation.

The mass block is subjected to gravitational force mg with g being gravitational acceleration, and the damping force $c\dot{\alpha}r$ with c being the damping coefficient. The governing equation that describes the mass block’s motion can be easily formulated as

$$\frac{d(mr^2\dot{\alpha})}{dt} = -mgr \sin \alpha - c \cdot \dot{\alpha} \cdot r^2 \tag{1}$$

in which

$$r(t) = \sqrt{L^2(t) - D^2}. \tag{2}$$

The combination of Equations (1) and (2) produces the following equation:

$$\frac{d[m(L^2(t) - D^2)\dot{\alpha}]}{dt} = -mg \left[\sqrt{L^2(t) - D^2} \right] \sin \alpha - c \cdot \dot{\alpha} \left[L^2(t) - D^2 \right]. \tag{3}$$

Equation (3) can be further converted to

$$\ddot{\alpha} = - \left[\frac{2L(t)\dot{L}(t)}{L^2(t) - D^2} + \frac{c}{m} \right] \dot{\alpha} - \frac{g}{\sqrt{L^2(t) - D^2}} \sin \alpha \tag{4}$$

where $\ddot{\alpha}$ and $\dot{L} \cos \theta$ denote $\frac{d^2\alpha}{dt^2}$ and $\frac{d(L \cos \theta)}{dt}$ of the block, respectively.

The elastic strain is assumed to be infinitesimal and is ignored. As a result, the fiber length can be related to the light-induced contraction:

$$L = L_0[1 + \varepsilon(t)]. \tag{5}$$

Combining Equations (3) and (5), we can obtain

$$r^2 = r_0^2 + L_0^2 \left[\varepsilon^2(t) + 2\varepsilon(t) \right]. \tag{6}$$

For the sake of simplifying the analysis, the fraction of cis-isomers within the LCE is assumed to be considerably less than 1. Hence, $\varepsilon(t)$ can be linked with $\phi(t)$ as

$$\varepsilon(t) = -C_0\phi(t) \tag{7}$$

with C_0 being the contraction coefficient. Inserting Equations (7) into (5) leads to

$$L = L_0[1 - C_0\phi(t)]. \tag{8}$$

2.2. Dynamic Model of the LCE Rope

To determine $\phi(t)$ in Equation (8), the dynamic LCE model put forward by Finkelmann et al. is used [74–76]. The *trans-to-cis* isomerization of LCE could be generated by UV or a laser with a wavelength less than 400 nm, according to the study by Yu et al. [77]. The thermal excitation from *trans* to *cis*, the thermally driven relaxation from *cis* to *trans*, and the light-driven relaxation from *trans* to *cis* together affect the number fraction $\phi(t)$ of *cis-isomers*. Since the thermal excitation from *trans* to *cis* is frequently thought to be minor as opposed to the light-driven excitation [76,78], the number fraction $\phi(t)$ can typically be described by the following governing equation.

$$\frac{\partial \phi}{\partial t} = \eta_0 I_0 (1 - \phi) - T_0^{-1} \phi \tag{9}$$

where T_0 is the thermal relaxation time from *cis* to *trans*, η_0 is the light absorption constant, and I_0 is the light intensity.

Solving Equation (9) by taking into account the initial conditions yields the following result

$$\phi(t) = \frac{\eta_0 T_0 I_0}{\eta_0 T_0 I_0 + 1} + \left(\phi_0 - \frac{\eta_0 T_0 I_0}{\eta_0 T_0 I_0 + 1} \right) \exp \left[-\frac{t}{T_0} (\eta_0 T_0 I_0 + 1) \right] \tag{10}$$

where ϕ_0 is the initial number fraction of *cis-isomers* at $t = 0$. Considering an initial number fraction of 0, i.e., $\phi_0 = 0$, Equation (10) can be simplified to

$$\phi(t) = \frac{\eta_0 T_0 I_0}{\eta_0 T_0 I_0 + 1} \left\{ 1 - \exp \left[-\frac{t}{T_0} (\eta_0 T_0 I_0 + 1) \right] \right\}. \tag{11}$$

For the case of LCE fiber exposed to the illumination, Equation (11) can be used to determine the number fraction of *cis-isomers*. Therefore, the contraction strain ε in LCE can be described as

$$\varepsilon = -C_0 \frac{\eta_0 T_0 I_0}{\eta_0 T_0 I_0 + 1} \left\{ 1 - \exp \left[-\frac{t}{T_0} (\eta_0 T_0 I_0 + 1) \right] \right\}. \tag{12}$$

For the case of the LCE fiber moving out of the illumination area, Equation (11) is alternatively expressed as

$$\phi(t) = \phi_0 \exp \left(-\frac{t}{T_0} \right) \tag{13}$$

in which ϕ_0 is its maximum within the light, and can be easily calculated as $\phi_0 = \frac{\eta_0 T_0 I_0}{\eta_0 T_0 I_0 + 1}$. Thus, it is possible to rewrite the number fraction of *cis-isomers* as

$$\phi(t) = \frac{\eta_0 T_0 I_0}{\eta_0 T_0 I_0 + 1} \exp \left(-\frac{t}{T_0} \right). \tag{14}$$

Then, the light-driven contraction strain ε in LCE can be expressed as

$$\varepsilon = -C_0 \frac{\eta_0 T_0 I_0}{\eta_0 T_0 I_0 + 1} \exp \left(-\frac{t}{T_0} \right). \tag{15}$$

2.3. Nondimensionalization

Dimensionless parameters like $\bar{t} = t/T_0$, $\bar{c} = cT_0/m$, $\bar{g} = gT_0^2/L_0$, $\bar{I} = \eta_0 T_0 I_0$, $\bar{L} = L/L_0$, and $\bar{D} = D/L_0$ are introduced to simplify the calculations. Accordingly, the dimensionless expressions of Equations (11) and (14) yield the following:

in the light,

$$\phi(\bar{t}) = 1 - \exp[-\bar{t}(\bar{I} + 1)] \tag{16}$$

and out of the light,

$$\phi(\bar{t}) = \exp(-\bar{t}). \tag{17}$$

Equations (16) and (17) govern the number fraction of *cis-isomers*. As the mass block moves across the boundary separating the illuminated and non-illuminated areas, the evolution law of $\phi(\bar{t})$ alternates between the behaviors described by Equations (16) and (17). It is worth mentioning that for Equation (16), $\phi(\bar{t})$ converges by keeping $\bar{I}_0 > 0$.

In the illumination zone,

$$\bar{\alpha} = - \left[\frac{2\bar{L}\bar{I}}{(\bar{L}^2 - \bar{D}^2)} + \bar{c} \right] \bar{\alpha} - \frac{\bar{g}}{\sqrt{\bar{L}^2 - \bar{D}^2}} \sin \alpha \tag{18}$$

where

$$\bar{L} = 1 - C_0 \frac{\bar{I}_0}{\bar{I}_0 + 1} \{1 - \exp[-\bar{t}(\bar{I}_0 + 1)]\} \tag{19}$$

$$\bar{\dot{L}} = -C_0 \bar{I}_0 \exp[-\bar{t}(\bar{I}_0 + 1)]. \tag{20}$$

In the non-illumination zone,

$$\bar{\ddot{\alpha}} = - \left[\frac{2\bar{L}\bar{\dot{L}}}{(\bar{L}^2 - \bar{D}^2)} + \bar{c} \right] \bar{\dot{\alpha}} - \frac{\bar{g}}{\sqrt{\bar{L}^2 - \bar{D}^2}} \sin \alpha \tag{21}$$

where

$$\bar{L} = 1 - C_0 \frac{\bar{I}_0}{\bar{I}_0 + 1} \exp(-\bar{t}) \tag{22}$$

$$\bar{\dot{L}} = C_0 \frac{\bar{I}_0}{\bar{I}_0 + 1} \exp(-\bar{t}) \tag{23}$$

where $\bar{\ddot{\alpha}}$ and $\bar{\dot{\alpha}}$ represent $\frac{d^2\bar{\alpha}}{d\bar{t}^2}$ and $\frac{d\bar{\alpha}}{d\bar{t}}$, respectively. In general, the governing equations are described by Equations (16) and (18)–(20) for the illumination zone, and Equations (17) and (21)–(23) for the dark zone.

2.4. Solution Method

Given that Equations (18) and (21) are differential equations with variable coefficients, we utilize the well-established fourth-order Runge–Kutta method for solving Equations (18) and (21) through MATLAB software (latest v R2023b). To facilitate this, Equations (18) and (21) are broken down into the following two-dimensional vector form: in the light,

$$\begin{pmatrix} \bar{\dot{\alpha}} \\ - \left[\frac{2\bar{L}\bar{\dot{L}}}{(\bar{L}^2 - \bar{D}^2)} + \bar{c} \right] \bar{\dot{\alpha}} - \frac{\bar{g}}{\sqrt{\bar{L}^2 - \bar{D}^2}} \sin \alpha \end{pmatrix} \tag{24}$$

in which,

$$\bar{L} = 1 - C_0 \frac{\bar{I}_0}{\bar{I}_0 + 1} \{1 - \exp[-\bar{t}(\bar{I}_0 + 1)]\} \tag{25}$$

$$\bar{\dot{L}} = -C_0 \bar{I}_0 \exp[-\bar{t}(\bar{I}_0 + 1)] \tag{26}$$

and out of the light,

$$\begin{pmatrix} \bar{\dot{\alpha}} \\ - \left[\frac{2\bar{L}\bar{\dot{L}}}{(\bar{L}^2 - \bar{D}^2)} + \bar{c} \right] \bar{\dot{\alpha}} - \frac{\bar{g}}{\sqrt{\bar{L}^2 - \bar{D}^2}} \sin \alpha \end{pmatrix} \tag{27}$$

in which,

$$\bar{L} = 1 - C_0 \frac{\bar{I}_0}{\bar{I}_0 + 1} \exp(-\bar{t}) \tag{28}$$

$$\bar{\dot{L}} = C_0 \frac{\bar{I}_0}{\bar{I}_0 + 1} \exp(-\bar{t}). \tag{29}$$

Finally, the iterative analysis is completed to identify the dynamic response of the rotation angle $\theta(\bar{t})$. The position α_{i+1} of the LCE fiber at time t_{i+1} is estimated through Equations (24)–(29). As a result, the dynamics of the LCE self-rotating skipping rope can be discovered for the given parameters $C_0, \bar{I}_0, \bar{c}, \bar{g}, \alpha_0, \bar{\alpha}_0,$ and β .

By building a model in MATLAB, we can describe the motion behavior of the LCE self-rotating skipping rope. Figure 2 displays its two motion states, namely the self-rotation state and static state. Among them, Figure 2a,b depict the time history and limit cycle of

the self-rotation state, respectively. The parameters are set to be $c = 0.02$, $\bar{I}_0 = 0.9$, $C_0 = 0.2$, $\beta = \frac{\pi}{6}$, $\bar{\alpha}_0 = 3$, $\alpha_0 = 0$, $\theta = \frac{\pi}{6}$, and $\bar{g} = 2.5$. As observed in the graph of the limit cycle, the velocity of the skipping rope eventually settles on a closed curve. In addition, Figure 2c,d depict the time history and limit cycle for the static state, respectively. The parameters are set to be $c = 0.06$, $\bar{I}_0 = 0.4$, $C_0 = 0.2$, $\beta = \frac{\pi}{6}$, $\bar{\alpha}_0 = 3$, $\alpha_0 = 0$, $\theta = \frac{\pi}{6}$, and $\bar{g} = 2.5$. The graph of the limit cycle demonstrates that the velocity of the skipping rope gradually diminishes and eventually stays at zero.

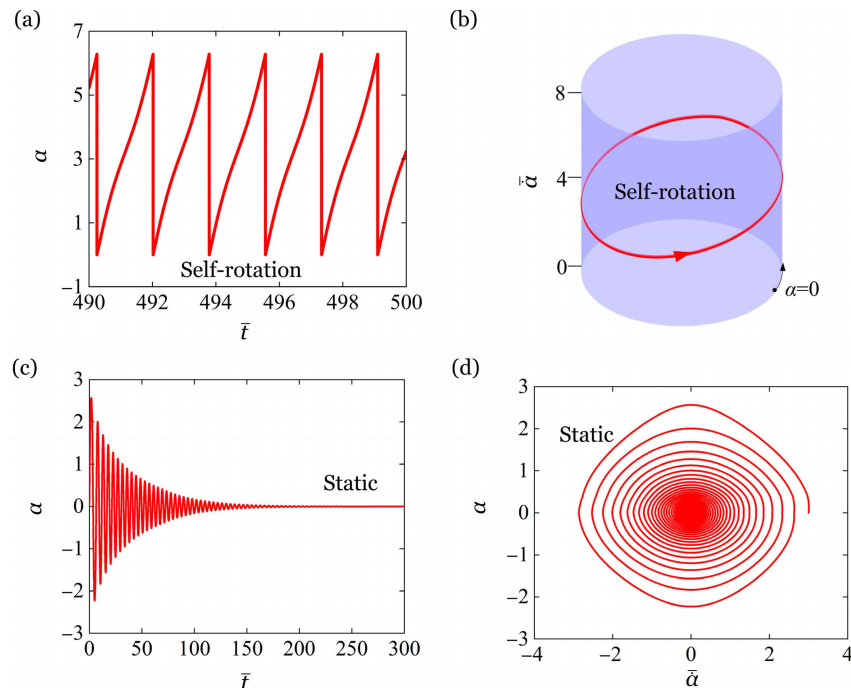


Figure 2. Two motion regimes of the skipping rope exposed to the constant light. (a) Time history for self-rotation state ($\bar{I}_0 = 0.9$, $c = 0.02$); (b) Limit cycle for self-rotation state; (c) Time history for static state ($\bar{I}_0 = 0.4$, $c = 0.06$); (d) Limit cycle for static state.

Accurate results can be obtained through MATLAB modeling calculations, but the numerical computations typically involve a complex process and lengthy calculation times, which are not conducive to inverse design. Therefore, it is necessary to find a more convenient and efficient calculation method.

3. RF and BPNN Modeling

For the theoretical model of the LCE self-rotating skipping rope, six system parameters have been identified as significant factors that affect its rotation frequency. These parameters are damping coefficient \bar{c} , light intensity \bar{I}_0 , illumination range β , initial velocity $\bar{\alpha}_0$, contraction coefficient C_0 , and gravitational acceleration \bar{g} . Given the analysis of the aforementioned theoretical model, the rotation frequency of the LCE self-rotating skipping rope can be determined when these six parameters are known. However, the presence of numerous parameter combinations in actual engineering complicates frequency calculations, making it impossible to determine parameter values inversely for a specific frequency. Machine learning can help solve this issue. In this section, the rotation frequency of the model will be predicted using machine learning.

3.1. RF and BPNN for Frequency Prediction and Parameter Inverse Design

Machine learning belongs to the field of Artificial Intelligence, which is a technical approach that enables machines to make decisions and predictions automatically by learning patterns and rules from data, without explicit programming. RF and BPNN algorithms are used in machine learning to address regression problems, and they have been selected

for frequency prediction and inverse design in the current study. BPNN can learn from complex nonlinear relationships in the data, while RF can process a large number of features and outliers to provide stable predictions. Therefore, we will employ RF and BPNN algorithms for prediction and comparison, respectively, to achieve higher accuracy and robustness. This combined approach will assist us to fully comprehend the data and provide reliable predictions, leading to superior outcomes in tasks such as frequency prediction and parameter inverse design.

As illustrated in Figure 3a, we input the combined parameters (refer to Table 1 for details) into MATLAB to perform frequency calculations and obtain 138,240 sets of data. These data will be fed to BPNN and RF algorithms for prediction and analysis.

RF is a machine learning algorithm based on an ensemble of decision trees. Referring to Figure 3b, the process involves constructing multiple decision trees by randomly sampling with replacement from the training dataset to create multiple subsets. Subsequently, feature subsampling is performed to select the feature subsets. During the construction of each decision tree, a feature selection algorithm is utilized to determine the splitting criterion at each node and iteratively generate child nodes. Finally, the outputs of these decision trees are combined to provide accurate predictions and classifications.

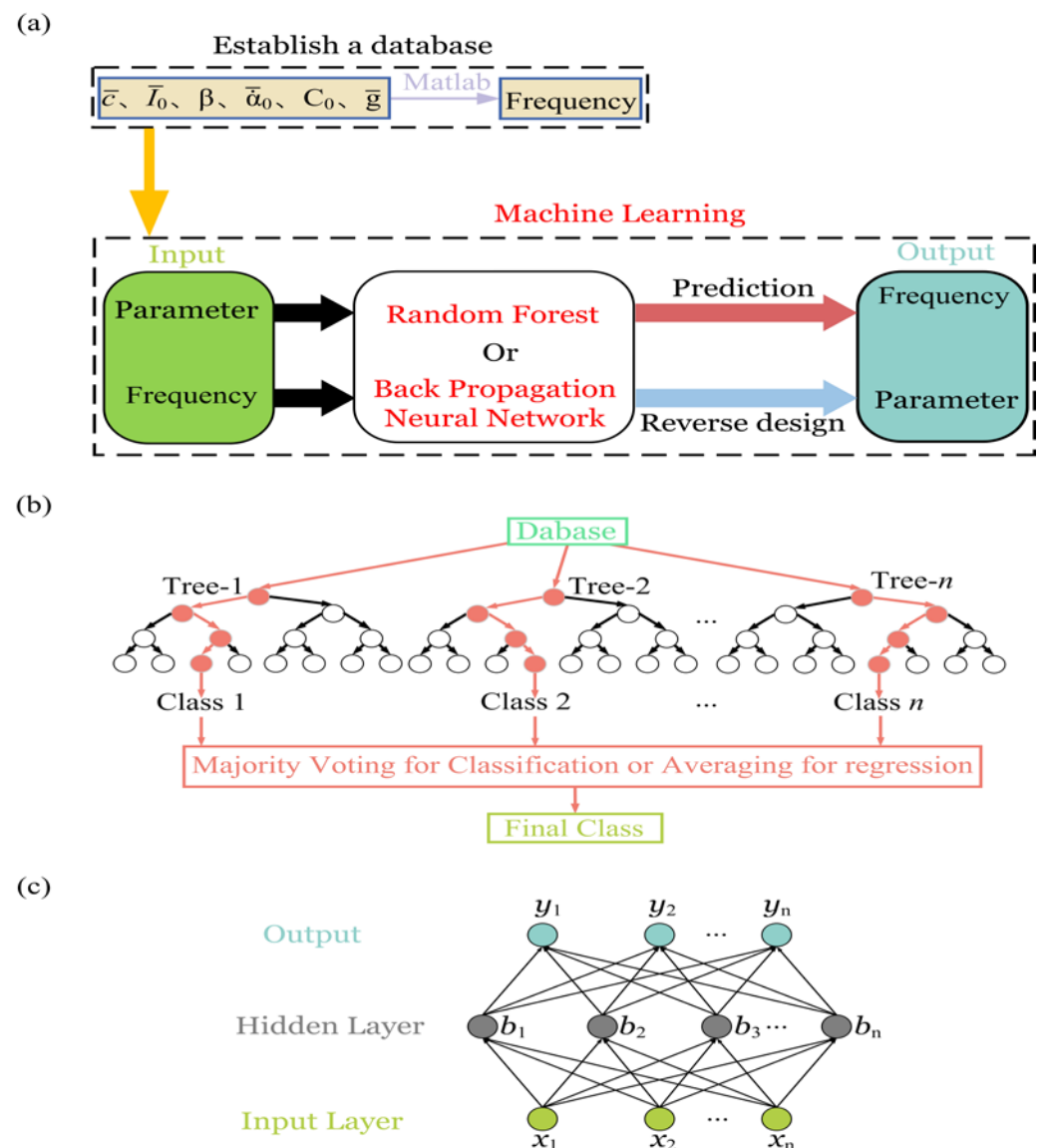


Figure 3. Architecture of RF and BPNN algorithms. (a) Database establishment and machine learning. (b) Principle of RF. (c) Principle of BPNN.

Table 1. Computational parameters of the training set and testing set.

Parameter	Training Set	Testing Set
\bar{c}	From 0.005 to 0.04 with a gradient of 0.005	From 0.012 to 0.034 with a gradient of 0.011
\bar{I}_0	From 0.1 to 0.8 with a gradient of 0.1	From 0.62 to 0.75 with a gradient of 0.5
β	From 10 to 170 with a gradient of 20	From 35 to 65 with a gradient of 10
C	From 0.1 to 0.6 with a gradient of 0.1	From 0.32 to 0.42 with a gradient of 0.5
$\bar{\delta}$	From 0.5 to 4 with a gradient of 0.5	From 1.8 to 2.8 with a gradient of 0.5
$\bar{\alpha}_0$	From 1 to 5 with a gradient of 1	From 2.5 to 3.5 with a gradient of 1

BPNN is a popular artificial neural network model. As exemplified in Figure 3c, the process involves initializing the network structure, performing forward propagation to generate predictions, calculating the error by comparing the predictions with the true labels, applying the backpropagation algorithm to update the network weights based on the error, and repeating these steps until the stopping condition is met. By iteratively adjusting the weights, BPNN learns patterns and correlations in the training data to make predictions and classifications for new input data. It is a supervised learning algorithm that finds applications in various machine learning and deep learning tasks.

In this study, the training and prediction of Random Forest and BPNN are realized through MATLAB software programming (latest v R2023b). In the training process, the training sample is first normalized and mapped to the range of [76,78]. A newff function in the Neural Network Toolbox of MATLAB is applied to construct the BPNN model, and the RF model is constructed by the TreeBagger function. For the training of BPNN, the network parameters `net.trainParam.epochs` = 10^3 , `net.trainParam.goal` = 10^{-6} , and `net.trainParam.lr` = 1^{-2} are used. For the training of RF, `trees` = 10^2 and `leaf` = 5 are configured as parameters. In the prediction process, the test samples are normalized first, then the `sim` function is used to simulate the trained BPNN model, and the `predict` function is used to simulate the trained Random Forest model. Finally, the simulation results are normalized and the final prediction results are obtained. This process combines the training and prediction steps of normalization, BPNN and RF models, and provides a comprehensive and systematic analysis framework for the research.

3.2. RF and BPNN Model Training and Evaluation

The RF and BPNN models are trained using the database and their training outcomes are subsequently evaluated using the determination coefficient R^2 , as derived from Equation (30). The R^2 value ranges from 0 to 1, with a higher value indicating a better fit between the model and the target variable. One hundred sets of data were randomly selected for visualization in Figure 4a,b. Both the RF and BPNN models achieved a score of 0.94, showcasing their excellent performance during training. Moreover, the RF model illustrates the degree of contribution of various parameters to the training outcomes, as shown in Figure 4e. In contrast, BPNNs are possibly the least interpretable methods and are often described as a black box, which means they are flexible but provide no insight into the structure of the function being approximated [79]. Therefore, from the perspective of interpretability of the model, the performance of an RF model is better than that of a BPNN model [80].

We also utilize the RF and BPNN models to predict the classification issue of whether the model is in a static or self-rotation state, and the prediction outcomes are depicted in Figure 4c,d. The prediction performance is evaluated in terms of accuracy calculated in accordance with Equation (31), yielding 95.83 for BPNN and 98.89 for RF. When addressing the classification issue, RF exhibits higher accuracy in predicting the motion states.

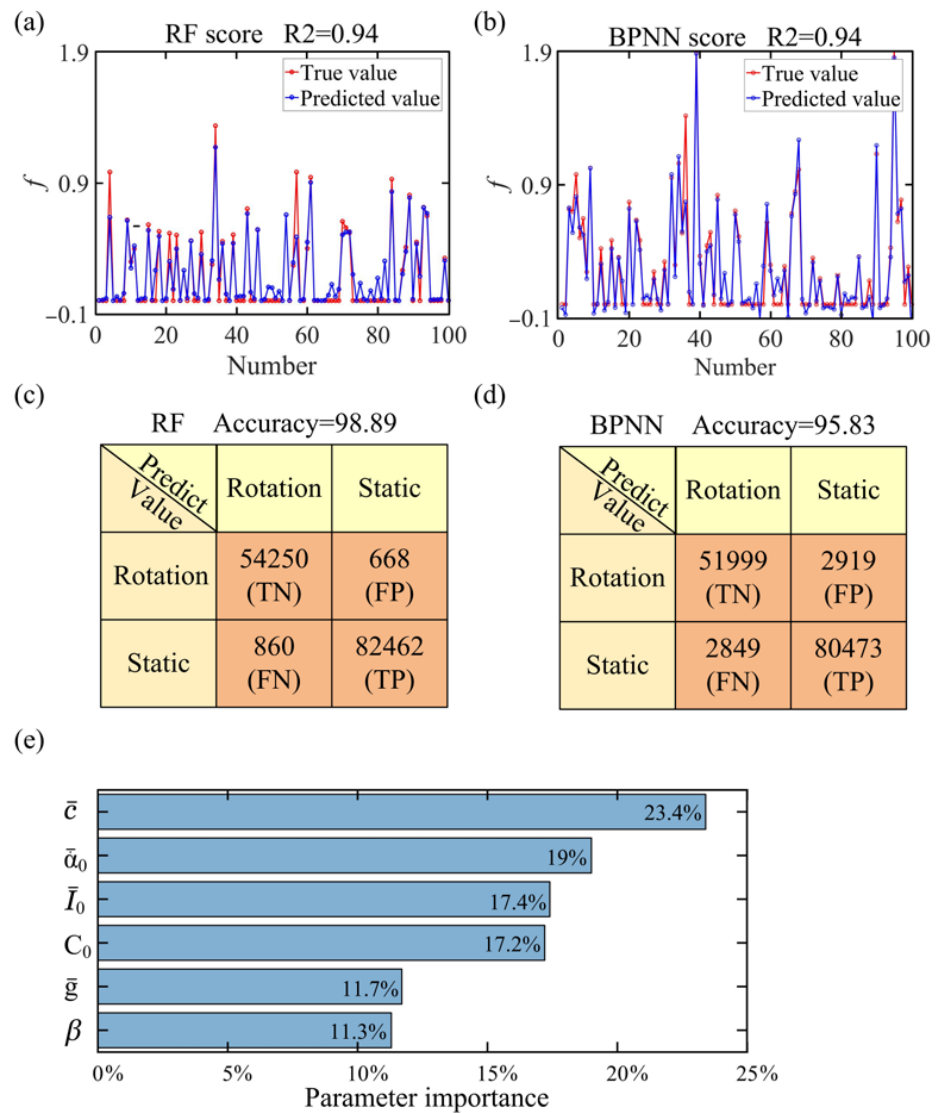


Figure 4. Validation for the rationality of RF and BPNN models: (a) RF training results for regression issues. (b) BPNN training results for regression issues. (c) Confusion matrix of RF. (d) Confusion matrix of BPNN. (e) Parameter contribution degree. Both algorithms perform well in training.

From the above experiments, it is apparent that both RF and BPNN models perform well during training, demonstrating high R² and accuracy. Notably, the RF model also provides insights into the significance of individual parameters in influencing the training outcomes, which can be valuable for optimizing the models. In brief, this approach not only reveals the extent to which features contribute to the prediction task but also assists researchers in selecting the most relevant features for further analysis and interpretation.

$$R^2 = 1 - \frac{\sum_{i=1}^n (f_i - \hat{f}_i)^2}{\sum_{i=1}^n (f_i - \bar{f}_i)^2} \tag{30}$$

where f_i is the true value, \bar{f}_i is the average of the true value, and \hat{f} is the predicted value.

$$\text{Accuracy} = \frac{TP + TN}{TP + TN + FP + FN} \tag{31}$$

where TP is True Positive, denoting the number of samples correctly predicted as positive by the model, TN is True Negative, denoting the number of samples correctly predicted as negative by the model, FP is False Positive, representing the number of samples incorrectly predicted as positive by the model, and FN is False Negative, representing the number of samples incorrectly predicted as negative by the model.

3.3. Generalization of RF and BPNN

After training, both the BPNN and RF models demonstrate impressive performance on the training set. To evaluate their generalization ability, we utilize a testing set of 1296 parameter combinations as presented in Table 1, which are different from the training data. The relative error (RE) between the predicted and true values is estimated using Equation (32), which is used to assess the extent of error. The differences between the predicted and true values for BPNN and RF are displayed in Figure 5a,c, respectively. We divide these 1296 datasets into four groups and estimate their relative errors, as shown in Figure 5b,d. The relative error for BPNN remains around 5%, while that for RF is approximately 10%. Since all 1296 datasets induce the system into a self-rotation state, no generalization testing is conducted to assess classification ability. It is evident from the outcomes that BPNN outperforms RF in terms of generalization ability. To sum up, our work demonstrates the potential and accuracy of both BPNN and RF in prediction, providing strong evidence to support further applications and research.

$$RE = \frac{\left(\sum_{i=1}^n \frac{|f_i - \hat{f}_i|}{f_i} \right)}{n} \times 100\% \tag{32}$$

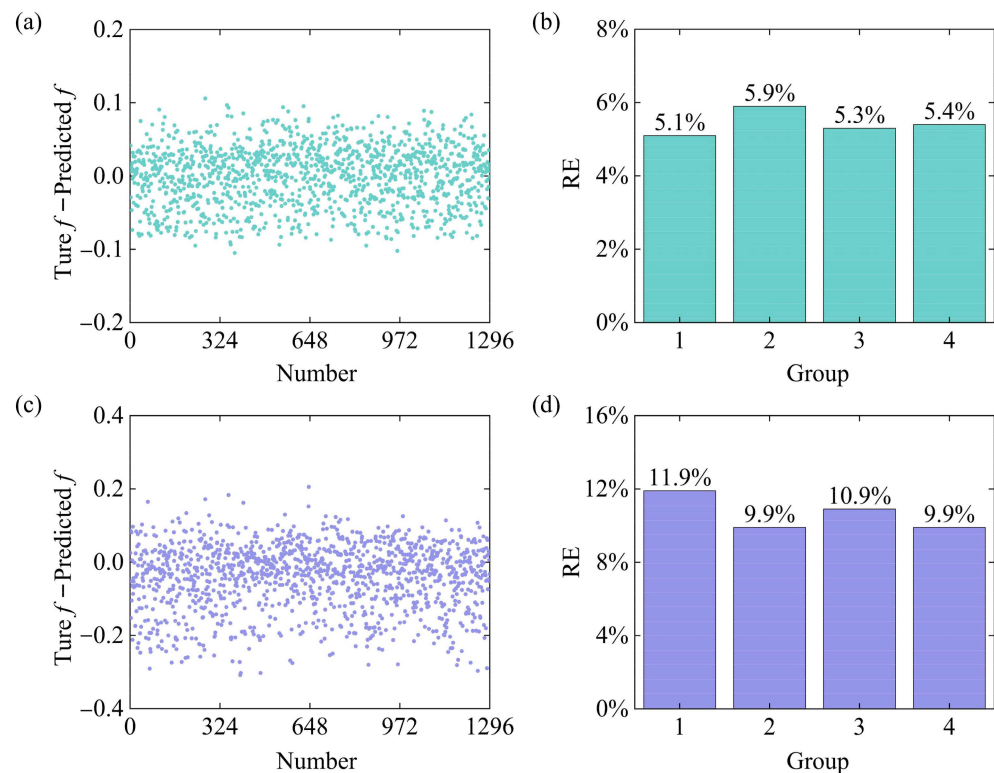


Figure 5. Analysis of the prediction outcomes: (a) Scatter plot of the difference between true and predicted values of BPNN. (b) Histogram of relative error of BPNN. (c) Scatter plot of the difference between true and predicted values of RF. (d) Histogram of relative error of RF. The generalization ability of BPNN is superior to that of RF.

4. Influences of System Parameters on Rotation Behavior

The above discussion allows us to summarize the motion states of the LCE skipping rope system. The implementation of these rules is governed by six dimensionless system parameters, including $\bar{\alpha}_0$, β , \bar{I}_0 , C_0 , \bar{c} , and \bar{g} . According to Equations (24)–(29), changing these parameters sequentially will bring about a range of results. This section applies RF to anticipate the motion state and BPNN to predict the rotation frequency, in an attempt to discover the intrinsic connection between the motion states.

Figure 6 reveals the influences of diverse parameters on the rotation frequency of the LCE self-rotating skipping rope, comprising the true and predicted curves. In the computation, the parameters are set to be $\alpha_0 = 0$, $\beta = \frac{\pi}{8}$ and the other parameters are shown in Table 2. Examining the data distribution, the influence level of distinct parameters on the rotation frequency is clear. Figure 6a plots the effect of the damping coefficient on the rotation frequency. The effect of light intensity on the rotation frequency is illustrated in Figure 6b. Figure 6c describes the influence of the illumination range on the rotation frequency. Figure 6d shows how the contraction coefficient C_0 affects the rotation frequency. The relationship between rotation frequency and gravitational acceleration is depicted in Figure 6e. The effect of initial angular velocity $\bar{\alpha}_0$ on the rotation frequency is given in Figure 6f. The results indicate that the motion pattern of the self-rotation is influenced by factors including \bar{I}_0 , β , \bar{c} , \bar{g} , and C_0 . Higher \bar{I}_0 , C_0 , and \bar{g} , or a lower \bar{c} , generally results in an increased self-rotation frequency. As the β expands, the rotation frequency first increases and then decreases. Additionally, the $\bar{\alpha}_0$ typically has no impact on the rotation frequency.

The forecasted outcomes of BPNN and RF closely align with the actual influence curve, and the trends are generally consistent. This suggests that BPNN and RF can be utilized for parametric discussion and analysis. These two algorithms can accurately predict the influence of each parameter on the rotation frequency in the self-rotation state. Hence, we can rely on BPNN and RF to examine the effects of different parameters on the system’s behavior, and further optimize and enhance our experimental design. This will provide insights into the properties of the self-rotation state and the physical mechanisms involved.

Table 2. System parameters.

Parameters	\bar{c}	\bar{I}_0	β	C_0	\bar{g}	$\bar{\alpha}_0$
Damping coefficient (Figure 6a)	/	0.87	$\pi/8$	0.21	2.1	4.3
Light intensity (Figure 6b)	0.018	/	$\pi/8$	0.21	2.1	4.3
Illumination range (Figure 6c)	0.018	0.87	/	0.21	2.1	4.3
Contraction coefficient (Figure 6d)	0.018	0.87	$\pi/8$	/	2.1	4.3
Gravitational acceleration (Figure 6e)	0.018	0.87	$\pi/8$	0.21	/	4.3
Initial angular velocity (Figure 6f)	0.018	0.87	$\pi/8$	0.21	2.1	/

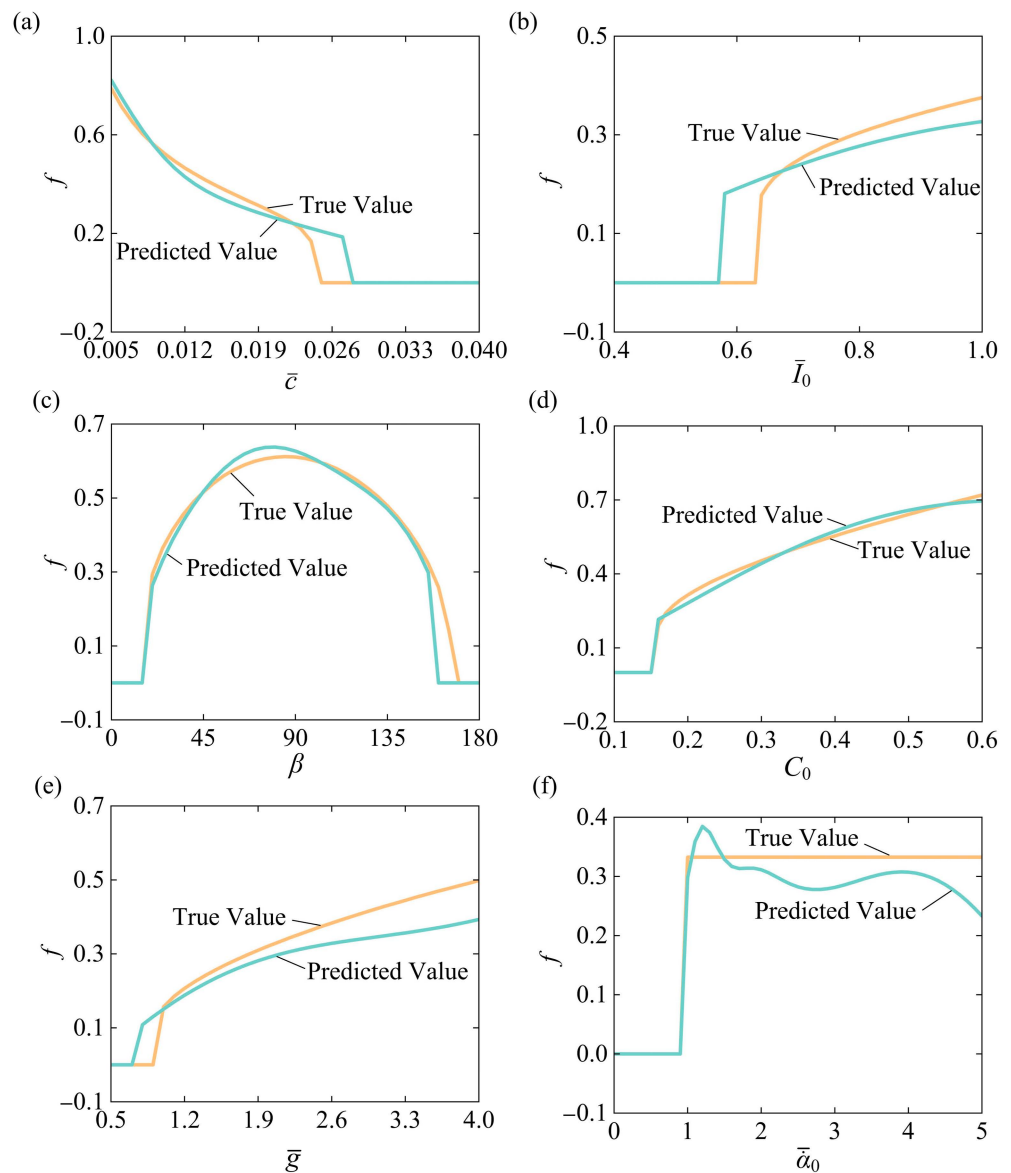


Figure 6. Influences of diverse parameters on rotation frequency. (a) Effect of damping coefficient \bar{c} on rotation frequency. (b) Effect of light intensity \bar{I}_0 on rotation frequency. (c) Effect of illumination range β on rotation frequency. (d) Effect of contraction coefficient C_0 on rotation frequency. (e) Effect of gravitational acceleration \bar{g} on rotation frequency. (f) Effect of initial angular velocity $\bar{\alpha}_0$ on rotation frequency. The predicted outcomes from BPNN and RF are highly correlated with the actual influence curve, with their trends being largely consistent.

5. Inverse Design

Practical engineering applications frequently necessitate the parameter predictions based on the obtained results. The focus of this section is to explore the inverse design of RF and BPNN algorithms for upgrading the accuracy of the remaining parameters at specific frequency and fixed parameters.

5.1. Inverse Design with No Fixed Parameters

Figure 7a illustrates the distribution of variances between the predicted and actual values. The true value is selected from the frequency obtained by running the parameter combinations from Table 1 in MATLAB. From the figure, the error of BPNN is observed to be in the range of 0.15 to 0.2, while that of RF ranges from 0.1 to 0.3. It appears that the predicted values are generally close to the true values, with only a slight deviation. For

in-depth analysis, we divide the data into four groups and estimate the relative error for each group, which is presented in Figure 7b,d. It is noticed that without accounting for fixed parameters, the relative error concentrates around 30% after using the rotation frequency for inverse design. This margin of error is remarkably similar to the error obtained when utilizing system parameters to predict the rotation frequency. Consequently, the feasibility and effectiveness of RF and BPNN are validated. These discoveries provide additional insights and confirm the reliability of the RF and BPNN algorithms in predicting and analyzing the behavior of the self-oscillatory system. The outcomes highlight the potential of this approach in optimizing the design and performance of such systems.

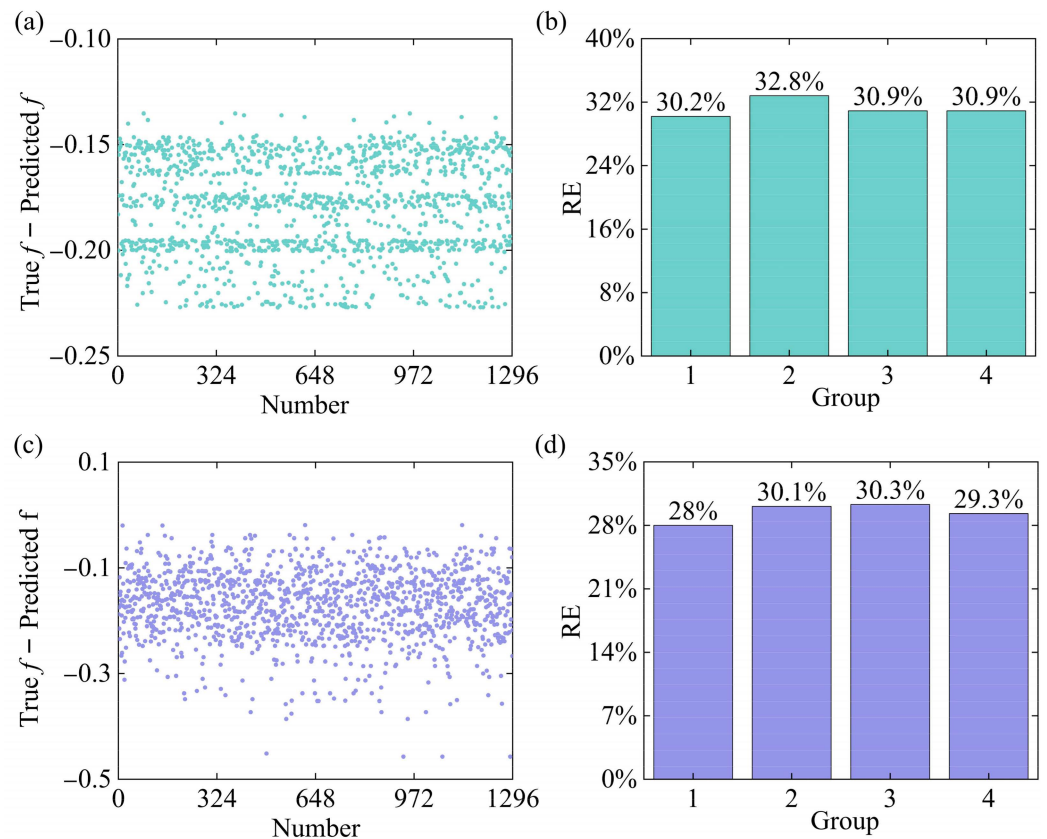


Figure 7. Error analysis of predicted versus true values for inverse design with no fixed parameters: (a) Scatter plot of the difference between true and predicted values of BPNN. (b) Histogram of relative error of BPNN. (c) Scatter plot of the difference between true and predicted values of RF. (d) Histogram of relative error of RF. The relative error is concentrated at about 30% after using the frequency for inverse design.

5.2. Inverse Design with Fixed Parameters

In practical engineering applications, certain parameters are usually fixed, such as the damping coefficient, contraction coefficient, and gravitational acceleration. However, others may be adjustable to some extent, like light intensity and the illumination range. With fixed parameters, RF and BPNN can be applied to predict light intensity and the illumination range.

We set the fixed parameters to $\bar{c} = 0.024$, $C_0 = 0.2$, $\bar{g} = 2$, and $\bar{\alpha}_0 = 3$. The choice of frequency is the same as stated in Section 5.1. After conducting the inverse design with fixed parameters, the error of the BPNN is significantly reduced, as depicted in Figure 8a, and the relative error is decreased to approximately 16%, as illustrated in Figure 8b. The error of RF, on the other hand, does not decline significantly, as shown in Figure 8c,d. These results imply that BPNN is more suitable for the inverse design of frequency than RF when fixed parameters are considered. BPNN is capable of constructing precise models by

capturing nonlinear relationships between the input parameters and the output frequency, whereas RF might be unable to effectively capture this nonlinear relationship, potentially leading to lower prediction accuracy.

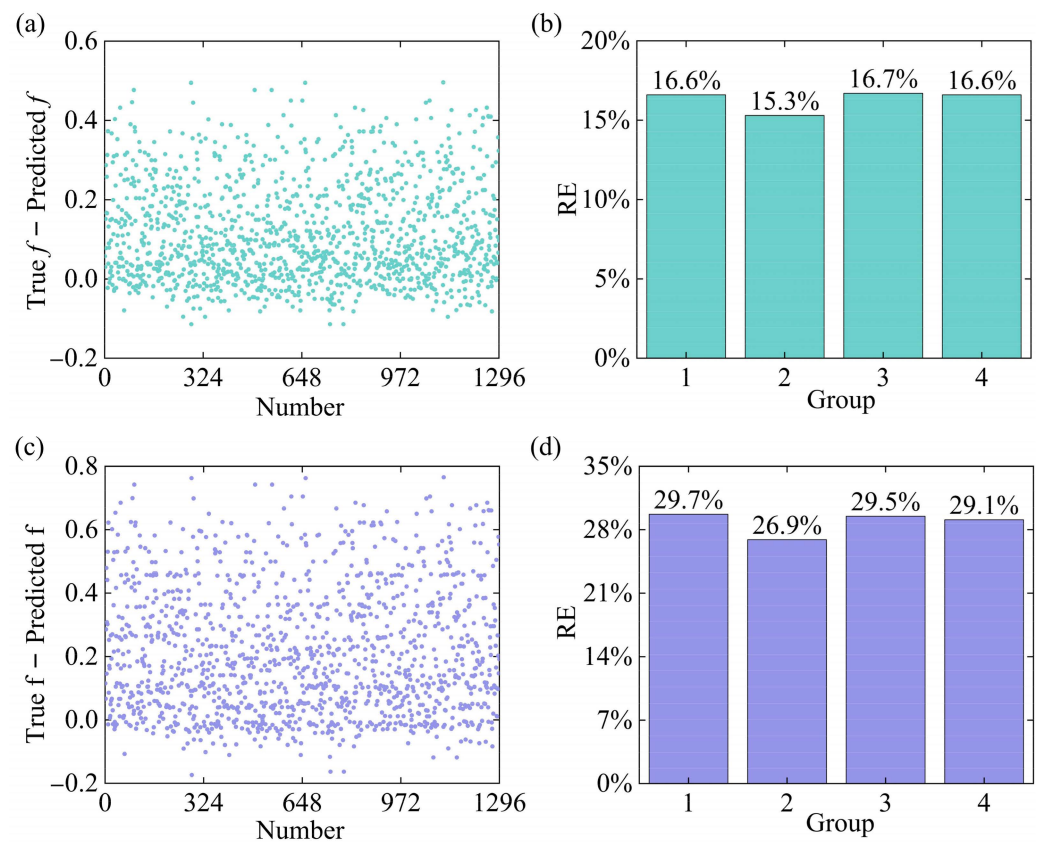


Figure 8. Error analysis of predicted and true values for inverse design with fixed parameters: (a) Scatter plot of the difference between true and predicted values of BPNN. (b) Histogram of relative error of BPNN. (c) Scatter plot of the difference between true and predicted values of RF. (d) Histogram of relative error of RF. After the inverse design with fixed parameters, the relative errors of RF and BPNN are around 30% and 16%, respectively.

By reducing errors and improving the accuracy of predictions, this approach enhances the reliability and precision of the inverse design process. The findings provide valuable insights into optimizing the design and performance of such systems under specific parameter configurations.

6. Concluding Remarks

The complexity of self-oscillatory systems, and their susceptibility to being influenced by multiple parameters simultaneously, present significant challenges to calculations, particularly in inverse parameter design. In the current study, a simple and effective approach is proposed to predict the rotation frequency of the LCE self-rotating skipping rope by combining theoretical modeling and machine learning. This method considers various parameters and can also inversely determine the parameters for a given frequency. Firstly, we establish a theoretical model of the LCE self-rotating skipping rope through formula derivation. The numerical solutions derived from this model are utilized as the training and testing data for RF and BPNN. By comparing the prediction outcomes of RF and BPNN with the training results, we confirm the accuracy of RF and BPNN, and draw the following conclusions:

- (1) Compared with the accurate results based on MATLAB, the prediction errors are approximately 10% for RF and around 5% for BPNN. This approach provides higher operating efficiency compared to MATLAB.
- (2) In terms of inverse design, BPNN demonstrates higher accuracy, indicating that BPNN can be effectively utilized for the inverse design of the rotation frequency of the LCE self-rotating skipping rope.

With its extensive application potential, this machine learning-based inverse design approach can be applied to address other similar issues, such as dynamical systems and nonlinear systems. This will provide an efficient and trustworthy tool for research and development in the domain of dynamical systems and nonlinear systems. Moreover, we can explore the implementation of additional machine learning algorithms or hybrid models to enhance the accuracy of predictions and designs. By incorporating various algorithms and models, we can expand the applicability of our approach to a wide range of complex scenarios and provide solutions for a broader array of engineering and scientific challenges.

Author Contributions: Conceptualization, Y.Q.; software, Y.Q. and H.W.; data curation, Y.Q.; writing—original draft, Y.Q. and Y.D.; validation, H.W., Y.D. and K.L.; writing—reviewing and editing, Y.D. and K.L.; supervision, K.L. All authors have read and agreed to the published version of the manuscript.

Funding: The authors acknowledge the support from the University Natural Science Research Project of Anhui Province (Nos. 2022AH020029 and 2022AH040042), the National Natural Science Foundation of China (No. 12172001), the Anhui Provincial Natural Science Foundation (Nos. 2208085Y01 and 2008085QA23), and the Housing and Urban-Rural Development Science and Technology Project of Anhui Province (No. 2023-YF129).

Data Availability Statement: The data presented in this study are available on request from the corresponding author.

Conflicts of Interest: The authors declare no conflict of interest.

References

1. Fu, M.; Burkart, T.; Maryshev, I.; Franquelim, H.G.; Merino-Salomón, A.; Reverte-López, M.; Frey, E.; Schwille, P. Mechanochemical feedback loop drives persistent motion of liposomes. *Nat. Phys.* **2023**, *19*, 1211–1218. [[CrossRef](#)]
2. Zheng, E.; Brandenbourger, M.; Robinet, L.; Schall, P.; Lerner, E.; Coulais, C. Self-Oscillation and Synchronization Transitions in Elastoactive Structures. *Phys. Rev. Lett.* **2023**, *130*, 178202. [[CrossRef](#)] [[PubMed](#)]
3. Ma, X.; Song, Y.; Cao, P.; Li, J.; Zhang, Z. Self-excited vibration suppression of a spline-shafting system using a nonlinear energy sink. *Int. J. Mech. Sci.* **2023**, *245*, 108105. [[CrossRef](#)]
4. Hua, M.; Kim, C.; Du, Y.; Wu, D.; Bai, R.; He, X. Swaying gel: Chemo-mechanical self-oscillation based on dynamic buckling. *Matter* **2021**, *4*, 1029–1041. [[CrossRef](#)]
5. Korner, K.; Kuenstler, A.S.; Hayward, R.C.; Audoly, B.; Bhattacharya, K. A nonlinear beam model of photomotile structures. *Proc. Natl. Acad. Sci. USA* **2020**, *117*, 9762–9770. [[CrossRef](#)] [[PubMed](#)]
6. Zhang, Z.; Duan, N.; Lin, C.; Hua, H. Coupled dynamic analysis of a heavily-loaded propulsion shafting system with continuous bearing-shaft friction. *Int. J. Mech. Sci.* **2020**, *172*, 105431. [[CrossRef](#)]
7. Li, S.; Peng, H.; Liu, C.; Ding, C.; Tang, H. Nonlinear characteristic and chip breaking mechanism for an axial low-frequency self-excited vibration drilling robot. *Int. J. Mech. Sci.* **2022**, *230*, 107561.
8. Niehues, J.; Jensen, G.G.; Haerter, J.O. Self-organized quantization and oscillations on continuous fixed-energy sandpiles. *Phys. Rev. E* **2022**, *105*, 034314. [[CrossRef](#)]
9. Wang, X.-Q.; Ho, G.W. Design of untethered soft material micromachine for life-like locomotion. *Mater. Today* **2022**, *53*, 197–216. [[CrossRef](#)]
10. Papangelo, A.; Putignano, C.; Hoffmann, N. Self-excited vibrations due to viscoelastic interactions. *Mech. Syst. Signal Process.* **2020**, *144*, 106894. [[CrossRef](#)]
11. He, Q.; Yin, R.; Hua, Y.; Jiao, W.; Mo, C.; Shu, H.; Raney, J.R. A modular strategy for distributed, embodied control of electronics-free soft robots. *Sci. Adv.* **2023**, *9*, eade9247. [[CrossRef](#)] [[PubMed](#)]
12. Dong, L.; Zhao, Y. Photothermally driven liquid crystal polymer actuators. *Mater. Chem. Front.* **2018**, *2*, 1932–1943. [[CrossRef](#)]
13. Chun, S.; Pang, C.; Cho, S.B. A Micropillar-Assisted Versatile Strategy for Highly Sensitive and Efficient Triboelectric Energy Generation under In-Plane Stimuli. *Adv. Mater.* **2020**, *32*, e1905539. [[CrossRef](#)] [[PubMed](#)]
14. He, X.; Aizenberg, M.; Kuksenok, O.; Zarzar, L.D.; Shastri, A.; Balazs, A.C.; Aizenberg, J. Synthetic homeostatic materials with chemo-mechano-chemical self-regulation. *Nature* **2012**, *487*, 214–218. [[CrossRef](#)] [[PubMed](#)]

15. Hu, W.; Lum, G.Z.; Mastrangeli, M.; Sitti, M. Small-scale soft-bodied robot with multimodal locomotion. *Nature* **2018**, *554*, 81–85. [[CrossRef](#)] [[PubMed](#)]
16. Haberl, J.M.; Sánchez-Ferrer, A.; Mihut, A.M.; Dietsch, H.; Hirt, A.M.; Mezzenga, R. Liquid-Crystalline Elastomer-Nanoparticle Hybrids with Reversible Switch of Magnetic Memory. *Adv. Mater.* **2013**, *25*, 1787–1791. [[CrossRef](#)] [[PubMed](#)]
17. Preston, D.J.; Rothmund, P.; Jiang, H.J.; Nemitz, M.P.; Rawson, J.; Suo, Z.; Whitesides, G.M. Digital logic for soft devices. *Proc. Natl. Acad. Sci. USA* **2019**, *116*, 7750–7759. [[CrossRef](#)]
18. Yang, X.; Shi, W.; Chen, Z.; Du, M.; Xiao, S.; Qu, S.; Li, C. Light-Fueled Nonequilibrium and Adaptable Hydrogels for Highly Tunable Autonomous Self-Oscillating Functions. *Adv. Funct. Mater.* **2023**, *33*, 2214394. [[CrossRef](#)]
19. Ding, Z.; Liu, Z.; Hu, J.; Swaddiwudhipong, S.; Yang, Z. Inhomogeneous large deformation study of temperature-sensitive hydrogel. *Int. J. Solids Struct.* **2013**, *50*, 2610–2619. [[CrossRef](#)]
20. Boissonade, J.; Kepper, P.D. Multiple types of spatio-temporal oscillations induced by differential diffusion in the Landolt reaction. *Phys. Chem. Chem. Phys.* **2011**, *13*, 4132–4137. [[CrossRef](#)] [[PubMed](#)]
21. Wu, J.; Yao, S.; Zhang, H.; Man, W.; Bai, Z.; Zhang, F.; Wang, X.; Fang, D.; Zhang, Y. Liquid crystal elastomer metamaterials with giant biaxial thermal shrinkage for enhancing skin regeneration. *Adv. Mater.* **2021**, *33*, 2170356. [[CrossRef](#)]
22. Wu, H.; Lou, J.; Dai, Y.; Zhang, B.; Li, K. Bifurcation analysis in liquid crystal elastomer spring self-oscillators under linear light fields. *Chaos Solitons Fractals* **2024**, *181*, 114587. [[CrossRef](#)]
23. Liu, J.; Shi, F.; Song, W.; Dai, Y.; Li, K. Modeling of self-oscillating flexible circuits based on liquid crystal elastomers. *Int. J. Mech. Sci.* **2024**, *270*, 109099. [[CrossRef](#)]
24. Dai, L.; Wang, L.; Chen, B.; Xu, Z.; Wang, Z.; Xiao, R. Shape memory behaviors of 3D printed liquid crystal elastomers. *Soft Sci.* **2023**, *3*, 4.
25. Wang, L.; Wei, Z.; Xu, Z.; Yu, Q.; Wu, Z.L.; Wang, Z.; Qian, J.; Xiao, R. Shape Morphing of 3D Printed Liquid Crystal Elastomer Structures with Precuts. *ACS Appl. Polym. Mater.* **2023**, *5*, 7477–7484. [[CrossRef](#)]
26. Wu, H.; Lou, J.; Zhang, B.; Dai, Y.; Li, K. Stability analysis of a liquid crystal elastomer self-oscillator under a linear temperature field. *Appl. Math. Mech.* **2024**, *45*, 337–354. [[CrossRef](#)]
27. Bai, C.; Kang, J.; Wang, Y.Q. Light-induced motion of three-dimensional pendulum with liquid crystal elastomeric fiber. *Int. J. Mech. Sci.* **2024**, *266*, 108911. [[CrossRef](#)]
28. Cheng, Y.; Lu, H.; Lee, X.; Zeng, H.; Priimagi, A. Kirigami-based light-induced shape-morphing and locomotion. *Adv. Mater.* **2019**, *32*, 1906233. [[CrossRef](#)] [[PubMed](#)]
29. Liao, B.; Zang, H.; Chen, M.; Wang, Y.; Lang, X.; Zhu, N.; Yang, Z.; Yi, Y. Soft Rod-Climbing Robot Inspired by Winding Locomotion of Snake. *Soft Robot.* **2020**, *7*, 500–511. [[CrossRef](#)]
30. Bazir, A.; Baumann, A.; Ziebert, F.; Kulić, I.M. Dynamics of fiberboids. *Soft Matter* **2020**, *16*, 5210–5223. [[CrossRef](#)] [[PubMed](#)]
31. Shin, B.; Ha, J.; Lee, M.; Park, K.; Park, G.H.; Choi, T.H.; Cho, K.-J.; Kim, H.-Y. Hygrobot: A self-locomotive ratcheted actuator powered by environmental humidity. *Sci. Robot.* **2018**, *3*, eaar2629. [[CrossRef](#)] [[PubMed](#)]
32. Hu, Y.; Ji, Q.; Huang, M.; Chang, L.; Zhang, C.; Wu, G.; Zi, B.; Bao, N.; Chen, W.; Wu, Y. Light-driven self-oscillating actuators with pototactic locomotion based on black phosphorus heterostructure. *Angew. Chem. Int. Ed.* **2021**, *60*, 20511–20517. [[CrossRef](#)] [[PubMed](#)]
33. Yang, H.; Zhang, C.; Chen, B.; Wang, Z.; Xu, Y.; Xiao, R. Bioinspired design of stimuli-responsive artificial muscles with multiple actuation modes. *Smart Mater. Struct.* **2023**, *32*, 085023. [[CrossRef](#)]
34. Manna, R.K.; Shklyaev, O.E.; Balazs, A.C. Chemical pumps and flexible sheets spontaneously form self-regulating oscillators in solution. *Proc. Natl. Acad. Sci. USA* **2021**, *118*, e2022987118. [[CrossRef](#)] [[PubMed](#)]
35. Li, Z.; Myung, N.V.; Yin, Y. Light-powered soft steam engines for self-adaptive oscillation and biomimetic swimming. *Sci. Robot.* **2021**, *6*, eabi4523. [[CrossRef](#)]
36. Xu, T.; Pei, D.; Yu, S.; Zhang, X.; Yi, M.; Li, C. Design of MXene Composites with Biomimetic Rapid and Self-Oscillating Actuation under Ambient Circumstances. *ACS Appl. Mater. Interfaces* **2021**, *13*, 31978–31985. [[CrossRef](#)]
37. da Cunha, M.P.; Peeketi, A.R.; Ramgopal, A.; Annabattula, R.K.; Schenning, A.P.H.J. Light-Driven Continual Oscillatory Rocking of a Polymer Film. *ChemistryOpen* **2020**, *9*, 1149–1152. [[CrossRef](#)] [[PubMed](#)]
38. He, Q.; Wang, Z.; Wang, Y.; Wang, Z.; Li, C.; Annapooranan, R.; Zeng, J.; Chen, R.; Cai, S. Electrospun liquid crystal elastomer microfiber actuator. *Sci. Robot.* **2021**, *6*, eabi9704. [[CrossRef](#)] [[PubMed](#)]
39. Hou, W.; Wang, J.; Lv, J. Bioinspired Liquid Crystalline Spinning Enables Scalable Fabrication of High-Performing Fibrous Artificial Muscles. *Adv. Mater.* **2023**, *35*, e2211800. [[CrossRef](#)] [[PubMed](#)]
40. Lahikainen, M.; Zeng, H.; Priimagi, A. Reconfigurable photoactuator through synergistic use of photochemical and photothermal effects. *Nat. Commun.* **2018**, *9*, 4148. [[CrossRef](#)]
41. Zhao, Y.; Chi, Y.; Hong, Y.; Li, Y.; Yang, S.; Yin, J. Twisting for soft intelligent autonomous robot in unstructured environments. *Proc. Natl. Acad. Sci. USA* **2022**, *119*, e2200265119. [[CrossRef](#)] [[PubMed](#)]
42. Cheng, Q.; Cheng, W.; Dai, Y.; Li, K. Self-oscillating floating of a spherical liquid crystal elastomer balloon under steady illumination. *Int. J. Mech. Sci.* **2023**, *241*, 107985. [[CrossRef](#)]
43. Serak, S.; Tabiryan, N.; Vergara, R.; White, T.J.; Vaia, R.A.; Bunning, T.J. Liquid crystalline polymer cantilever oscillators fueled by light. *Soft Matter* **2010**, *6*, 779–783. [[CrossRef](#)]

44. Zhao, D.; Liu, Y. A prototype for light-electric harvester based on light sensitive liquid crystal elastomer cantilever. *Energy* **2020**, *198*, 117351. [[CrossRef](#)]
45. Gelebart, A.H.; Mulder, D.J.; Varga, M.; Konya, A.; Ghislaine, V.; Meijer, E.W.; Selinger, R.L.B.; Broer, D.J. Making waves in a photoactive polymer film. *Nature* **2017**, *546*, 632–636. [[CrossRef](#)] [[PubMed](#)]
46. Zhao, T.; Fan, Y.; Lv, J.-A. Photomorphogenesis of Diverse Autonomous Traveling Waves in a Monolithic Soft Artificial Muscle. *ACS Appl. Mater. Interfaces* **2022**, *14*, 23839–23849. [[CrossRef](#)] [[PubMed](#)]
47. Shen, B.; Kang, S.H. Designing self-oscillating matter. *Matter* **2021**, *4*, 766–769. [[CrossRef](#)]
48. Graeber, G.; Regulagadda, K.; Hodel, P.; Küttel, C.; Landolf, D.; Schutzius, T.M.; Poulikakos, D. Leidenfrost droplet trampolining. *Nat. Commun.* **2021**, *12*, 1727. [[CrossRef](#)] [[PubMed](#)]
49. Kim, Y.; Berg, J.v.D.; Crosby, A.J. Autonomous snapping and jumping polymer gels. *Nat. Mater.* **2021**, *20*, 1695–1701. [[CrossRef](#)] [[PubMed](#)]
50. Hu, J.; Nie, Z.; Wang, M.; Liu, Z.; Huang, S.; Yang, H. Springtail-inspired Light-driven Soft Jumping Robots Based on Liquid Crystal Elastomers with Monolithic Three-leaf Panel Fold Structure. *Angew. Chem. Int. Ed.* **2023**, *62*, e202218227. [[CrossRef](#)]
51. Lv, X.; Yu, M.; Wang, W.; Yu, H. Photothermal pneumatic wheel with high loadbearing capacity. *Compos. Commun.* **2021**, *24*, 100651. [[CrossRef](#)]
52. Yu, Y.; Hu, H.; Dai, Y.; Li, K. Modeling the light-powered self-rotation of a liquid crystal elastomer fiber-based engine. *Phys. Rev. E* **2024**, *109*, 034701. [[CrossRef](#)]
53. Yu, Y.; Hu, H.; Wu, H.Y.; Dai, Y.T.; Li, K. A light-powered self-rotating liquid crystal elastomer drill. *Heliyon* **2024**, *10*, e27748. [[CrossRef](#)]
54. Xu, P.; Chen, Y.; Wu, H.; Dai, Y.; Li, K. Chaotic motion behaviors of liquid crystal elastomer pendulum under periodic illumination. *Results Phys.* **2024**, *56*, 107332. [[CrossRef](#)]
55. Baumann, A.; Sánchez-Ferrer, A.; Jacomine, L.; Martinoty, P.; Le Houerou, V.; Ziebert, F.; Kulić, I.M. Motorizing fibers with geometric zero-energy modes. *Nat. Mater.* **2018**, *17*, 523. [[CrossRef](#)] [[PubMed](#)]
56. Hu, Z.; Li, Y.; Lv, J.-A. Phototunable self-oscillating system driven by a self-winding fiber actuator. *Nat. Commun.* **2021**, *12*, 3211. [[CrossRef](#)] [[PubMed](#)]
57. Wu, H.; Zhang, B.; Li, K. Synchronous behaviors of three coupled liquid crystal elastomer-based spring oscillators under linear temperature fields. *Phys. Rev. E* **2024**, *109*, 024701. [[CrossRef](#)] [[PubMed](#)]
58. Kuenstler, A.S.; Chen, Y.; Bui, P.; Kim, H.; DeSimone, A.; Jin, L.; Hayward, R.C. Blueprinting Photothermal Shape-Morphing of Liquid Crystal Elastomers. *Adv. Mater.* **2020**, *32*, 2000609. [[CrossRef](#)]
59. Chen, B.; Liu, C.; Xu, Z.; Wang, Z.; Xiao, R. Modeling the thermo-responsive behaviors of polydomain and monodomain nematic liquid crystal elastomers. *Mech. Mater.* **2024**, *188*, 1048383. [[CrossRef](#)]
60. Liao, W.; Yang, Z. The Integration of Sensing and Actuating based on a Simple Design Fiber Actuator towards Intelligent Soft Robots. *Adv. Mater. Technol.* **2022**, *7*, 2101260. [[CrossRef](#)]
61. Sun, J.; Wang, Y.; Liao, W.; Yang, Z. Ultrafast, High-Contractile Electrothermal-Driven Liquid Crystal Elastomer Fibers towards Artificial Muscles. *Small* **2021**, *17*, 2103700. [[CrossRef](#)] [[PubMed](#)]
62. Hauser, A.W.; Sundaram, S.; Hayward, R.C. Photothermocapillary Oscillators. *Phys. Rev. Lett.* **2018**, *121*, 158001. [[CrossRef](#)] [[PubMed](#)]
63. Kim, H.; Sundaram, S.; Kang, J.-H.; Tanjeem, N.; Emrick, T.; Hayward, R.C. Coupled oscillation and spinning of photothermal particles in Marangoni optical traps. *Proc. Natl. Acad. Sci. USA* **2021**, *118*, e2024581118. [[CrossRef](#)] [[PubMed](#)]
64. Wang, Y.; Dang, A.; Zhang, Z.; Yin, R.; Gao, Y.; Feng, L.; Yang, S. Repeatable and Reprogrammable Shape Morphing from Photoresponsive Gold Nanorod/Liquid Crystal Elastomers. *Adv. Mater.* **2020**, *32*, e2004270. [[CrossRef](#)] [[PubMed](#)]
65. Wang, Y.; Yin, R.; Jin, L.; Liu, M.; Gao, Y.; Raney, J.; Yang, S. 3D-Printed Photoresponsive Liquid Crystal Elastomer Composites for Free-Form Actuation. *Adv. Funct. Mater.* **2023**, *33*, 2210614. [[CrossRef](#)]
66. Wang, R.; Bi, H.Y. A predictive model for Chinese children with developmental dyslexia—Based on a genetic algorithm optimized back-propagation neural network. *Expert Syst. Appl.* **2022**, *187*, 115949. [[CrossRef](#)]
67. Giri, S.; Kang, Y.; MacDonald, K.; Tippett, M.; Qiu, Z.; Lathrop, R.G.; Obropta, C.C. Revealing the sources of arsenic in private well water using Random Forest Classification and Regression. *Sci. Total Environ.* **2023**, *857*, 159360. [[CrossRef](#)] [[PubMed](#)]
68. Zhao, J.; Yan, H.; Huang, L. A joint method of spatial-spectral features and BP neural network for hyperspectral image classification. *Egypt. J. Remote Sens. Space Sci.* **2023**, *26*, 107–115. [[CrossRef](#)]
69. Chen, H.; Wu, L.; Chen, J.; Lu, W.; Ding, J. A comparative study of automated legal text classification using random forests and deep learning. *Inf. Process. Manag.* **2022**, *59*, 102798. [[CrossRef](#)]
70. Georgescu, P.-L.; Moldovanu, S.; Iticescu, C.; Calmuc, M.; Calmuc, V.; Topa, C.; Moraru, L. Assessing and forecasting water quality in the Danube River by using neural network approaches. *Sci. Total Environ.* **2023**, *879*, 162998. [[CrossRef](#)] [[PubMed](#)]
71. Li, K.; Qiu, Y.; Dai, Y.; Yu, Y. Modeling the dynamic response of a light-powered self-rotating liquid crystal elastomer-based system. *Int. J. Mech. Sci.* **2024**, *263*, 108794. [[CrossRef](#)]
72. Camacho-Lopez, M.; Finkelmann, H.; Palfy-Muhoray, P.; Shelley, M. Fast liquid-crystal elastomer swims into the dark. *Nat. Mater.* **2004**, *3*, 307–310. [[CrossRef](#)] [[PubMed](#)]
73. Marshall, J.E.; Terentjev, E.M. Photo-sensitivity of dye-doped liquid crystal elastomers. *Soft Matter* **2013**, *9*, 8547–8551. [[CrossRef](#)]

74. Hogan, P.M.; Tajbakhsh, A.R.; Terentjev, E.M. uv manipulation of order and macroscopic shape in nematic elastomers. *Phys. Rev. E* **2002**, *65*, 041720. [[CrossRef](#)] [[PubMed](#)]
75. Finkelmann, H.; Nishikawa, E.; Pereira, G.G.; Warner, M. A New Opto-Mechanical Effect in Solids. *Phys. Rev. Lett.* **2001**, *87*, 015501. [[CrossRef](#)] [[PubMed](#)]
76. Herbert, K.M.; Fowler, H.E.; McCracken, J.M.; Schlafmann, K.R.; Koch, J.A.; White, T.J. Synthesis and alignment of liquid crystalline elastomers. *Nat. Rev. Mater.* **2021**, *7*, 23–38. [[CrossRef](#)]
77. Yu, Y.; Nakano, M.; Ikeda, T. Photomechanics: Directed bending of a polymer film by light-miniaturizing a simple photomechanical system could expand its range of applications. *Nature* **2003**, *425*, 145. [[CrossRef](#)] [[PubMed](#)]
78. Nägele, T.; Hoche, R.; Zinth, W.; Wachtveitl, J. Femtosecond photoisomerization of cis-azobenzene. *Chem. Phys. Lett.* **1997**, *272*, 489–495. [[CrossRef](#)]
79. Østergård, T.; Jensen, R.L.; Maagaard, S.E. A comparison of six metamodeling techniques applied to building performance simulations. *Appl. Energy* **2018**, *211*, 89–103. [[CrossRef](#)]
80. Lu, S.; Li, Q.; Bai, L.; Wang, R. Performance predictions of ground source heat pump system based on random forest and back propagation neural network models. *Energy Convers. Manag.* **2019**, *197*, 111864. [[CrossRef](#)]

Disclaimer/Publisher’s Note: The statements, opinions and data contained in all publications are solely those of the individual author(s) and contributor(s) and not of MDPI and/or the editor(s). MDPI and/or the editor(s) disclaim responsibility for any injury to people or property resulting from any ideas, methods, instructions or products referred to in the content.